ELSEVIER

Contents lists available at ScienceDirect

# Journal of Materials Research and Technology

journal homepage: www.elsevier.com/locate/jmrt





# Achieving an excellent combination of strength and ductility in a single-phase metastable medium-entropy alloy

Caixia Wang <sup>a</sup>, Ruixing Sheng <sup>a</sup>, Dawei Zhou <sup>a</sup>, Weidong Li <sup>b,\*\*</sup>, Shuying Chen <sup>a,\*\*\*</sup>, Fanchao Meng <sup>a</sup>, Gihan Velisa <sup>c</sup>, Daiyi Chao <sup>d,\*\*\*\*</sup>, Liang Jiang <sup>a</sup>, Peter K. Liaw <sup>e,\*\*\*\*\*</sup>, Yang Tong <sup>a,\*</sup>

- <sup>a</sup> Institute for Advanced Studies in Precision Materials, Yantai University, Yantai, Shandong, 264005, China
- b Beijing Advanced Innovation Center for Materials Genome Engineering, University of Science and Technology Beijing, Beijing, 100083, China
- <sup>c</sup> Horia Hulubei National Institute for Physics and Nuclear Engineering, Măgurele, IF, 077125, Romania
- d Shandong Institutes of Industrial Technology, Yantai, Shandong, 264000, China
- <sup>e</sup> Department of Materials Science and Engineering, University of Tennessee, Knoxville, TN, 37996, USA

#### ARTICLE INFO

Handling editor: SN Monteiro

Keywords:
Medium-entropy alloy
Cryogenic deformation
Transmission electron microscopy
Strength-ductility balance

#### ABSTRACT

The development of robust alloys capable of maintaining high strength and ductility at cryogenic temperatures has been a long-sought goal, particularly for load-bearing applications in extremely low-temperature environments. In this study, we reported a newly developed face-centered-cubic (FCC) metastable (Ni $_{0.3}$ Co $_{0.4}$ Cr $_{0.3}$ ) $_{94}$ Mo $_{6}$  medium-entropy alloy (Mo-MEA) with an excellent synergy of strength and ductility at 77 K, surpassing the toughest equiatomic NiCoCr MEA. Compared to the equiatomic NiCoCr MEA, the Mo-MEA exhibited a substantial increase in yield strength by 68 % (from 407 to 685 MPa) and a decent enhancement of the ultimate tensile strength by 10 % (from 1289 to 1415 MPa), along with a marginal increase in elongation from 75 % to 78.45 %. Electron backscatter diffraction and transmission electron microscopy revealed the activation of multimodal deformation mechanisms, including dislocations, stacking faults, twinning, and FCC-to-hexagonal-close-packed phase transformation, during the tensile deformation at 77 K.

#### 1. Introduction

The selection of materials with a superior combination of strength and ductility is a crucial requirement for load-bearing applications at low temperatures. Insufficient toughness may cause catastrophic failure since metallic materials often display diminished toughness at reduced temperatures especially within the cryogenic temperature range [1,2]. Medium-entropy alloys (MEAs) are a new type of alloys consisting of three or four elements in an equiatomic or near-equiatomic fraction [3, 4]. Out of a variety of MEAs, the single-phase face-centered-cubic (FCC) NiCoCr MEA is the most studied due to its extraordinary enhancement of both strength and ductility with the decreasing temperature down to cryogenic temperature range [5–8]. Also, Liu et al. [9] recently have

reported the highest crack-growth fracture toughness, 540 MPa  $m^{1/2}$  at 20 K, in the equiatomic NiCoCr MEA, superior to the Cantor alloy, NiCoCrFeMn [10,11]. Ab initio calculations [12,13] have revealed that the NiCoCr MEA has an extremely low intrinsic stacking fault energy (SFE),  $-24~{\rm mJ/m^2}$  at 300 K, and prefers the hexagonal-close-packed (HCP) structure over FCC. Transmission electron microscopic (TEM) characterizations have revealed that multiple deformation mechanisms, including dislocations, stacking fault (SF), and twinning-induced plasticity (TWIP), were activated consequently during the deformation of the metastable FCC NiCoCr MEA at 77 K [6], and the transformation-induced plasticity (TRIP) mechanism was further triggered at 20 K [9]. The exceptional damage tolerance of the NiCoCr alloy is encouraging to the development of advanced alloys for applications in

E-mail addresses: wli20@utk.edu (W. Li), sychen@ytu.edu.cn (S. Chen), cdy19861226@163.com (D. Chao), Pliaw@utk.edu (P.K. Liaw), yt1@ytu.edu.cn (Y. Tong).

https://doi.org/10.1016/j.jmrt.2023.10.242

Received 19 August 2023; Received in revised form 19 October 2023; Accepted 23 October 2023 Available online 4 November 2023

2238-7854/© 2023 The Authors. Published by Elsevier B.V. This is an open access article under the CC BY-NC-ND license (http://creativecommons.org/licenses/by-nc-nd/4.0/).

<sup>\*</sup> Corresponding author.

<sup>\*\*</sup> Corresponding author.

<sup>\*\*\*</sup> Corresponding author.

<sup>\*\*\*\*</sup> Corresponding author.

<sup>\*\*\*\*\*</sup> Corresponding author.

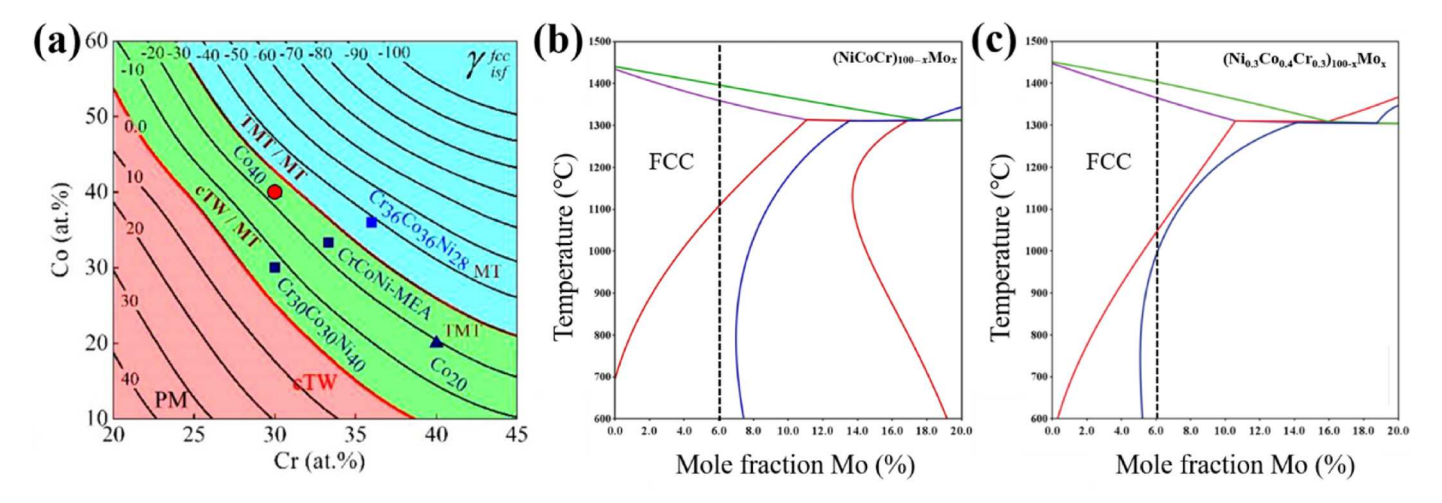


Fig. 1. (a) Correlation between predicted SFEs and compositions of Ni–Co–Cr alloy system at RT [12]. The region in red indicates alloys with the conventional twinning deformation mechanism (cTW), the blue one refers to TRIP deformation (or Martensitic transformation, MT), and the green one represents TMT deformation mechanism. The red dot indicates the Ni<sub>30</sub>Co<sub>40</sub>Cr<sub>30</sub> MEA. Computed phase diagrams of (NiCoCr)<sub>100-x</sub>Mo<sub>x</sub> (0  $\leq$  X  $\leq$  20) (b) (Ni<sub>0-3</sub>Co<sub>0-4</sub>Cr<sub>0.3</sub>)<sub>100-x</sub>Mo<sub>x</sub> (0  $\leq$  X  $\leq$  20) (c) MEA systems. The equilibrium phase diagram versus temperature was calculated by using thermos-calc software.

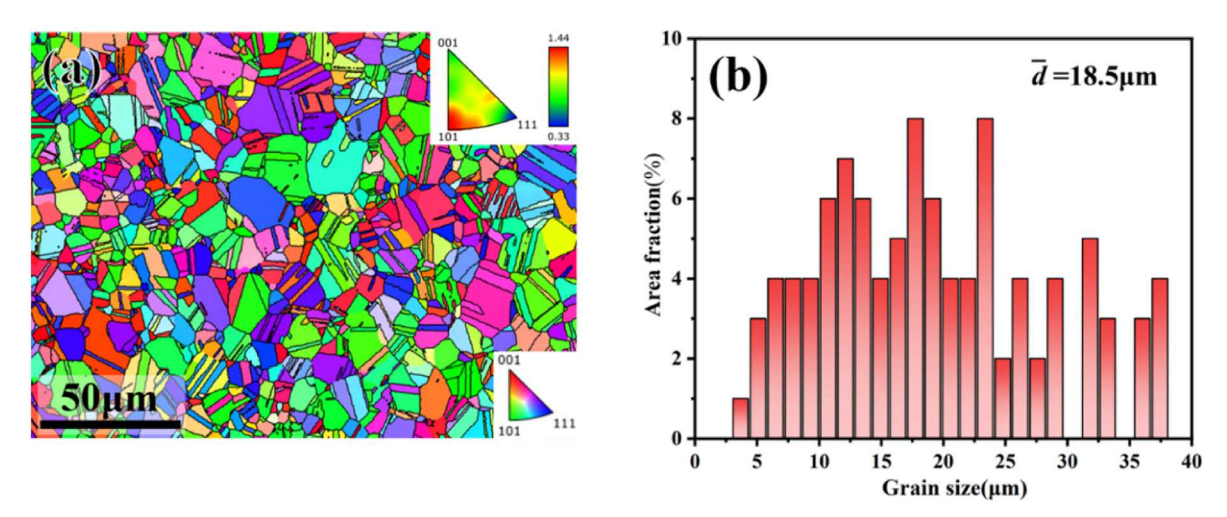


Fig. 2. EBSD analysis of microstructure of the Mo-MEA. (a) Inverse pole figure (IPF) and (b) grain-size distribution. The inset in the upper right of (a) shows the distribution of grain orientations.

#### extreme environments.

However, the equiatomic NiCoCr MEA is not necessarily the optimal candidate in the Ni-Co-Cr system for cryogenic temperature applications. In searching for Ni-Co-Cr MEA compositions to achieve high strength and ductility, a low SFE value is frequently used as an empirical guide. However, excessively low SFE values can increase the fraction of TRIP deformation and provoke ductility loss due to stress concentration at the HCP interfaces, as exemplified by the early fracture in the Ni<sub>20</sub>Co<sub>60</sub>Cr<sub>20</sub> MEA [14]. Using ab initio calculations, Yang et al. [12] examined the SFE of the Ni-Co-Cr MEA system covering a broad compositional space (Fig. 1a). Besides conventional TWIP deformation (cTW; red region in Fig. 1a) and TRIP deformation (martensitic transformation, MT; blue region in Fig. 1a) regions, Yang et al. [12] defined the third deformation region (the green one in Fig. 1a), phase transformation-mediated twinning (TMT). TMT involves an initial FCC-to-HCP martensitic transformation driven by a negative SFE, followed by partial dislocations traveling on basal planes, finally leading to the formation of FCC twin. The two-step twinning process sheds light on the improvement of ductility by consuming HCP phase. The equiatomic NiCoCr MEA is situated on the left side of the boundary between the TMT and MT deformation regions [12]. Yang et al. [12] further found

that the  $\rm Ni_{28}Co_{36}Cr_{36}$  MEA located on the right side of the TMT/MT boundary has an improved ultimate tensile strength without ductility compromise. Therefore, adding more Co and Cr to reduce the SFE should be done judiciously to limit TRIP deformation and achieve a balance between reasonable strength and good ductility.

However, the incremental enhancement in strength achieved by augmenting the Co and Cr content in the NiCoCr to form Ni<sub>28</sub>Co<sub>36</sub>Cr<sub>36</sub> MEA is relatively modest [12]. To achieve a synergistic combination of exceptional strength and excellent ductility in single-phase Ni-Co-Cr MEAs, it becomes imperative to explore the incorporation of alloying elements that can effectively reduce the SFE and induce robust solid-solution strengthening. A number of researches [15-21] about the introduction of strengthening elements, e.g., Mo, La, Y and Gd, into the NiCoCr MEA have been conducted to examine the phase evolution and mechanical properties at room temperature (RT). Previous investigations [15,19-22] have indicated that at RT the introduction of Mo into Ni-based MEAs not only imparts substantial solid-solution strengthening but also efficiently diminishes the SFE, even with a minor Mo addition. Prior investigation, however, have primarily concentrated on precipitation strengthening approach to enhance the strength of the extensively studied CrCoNi MEA, particularly at RT.

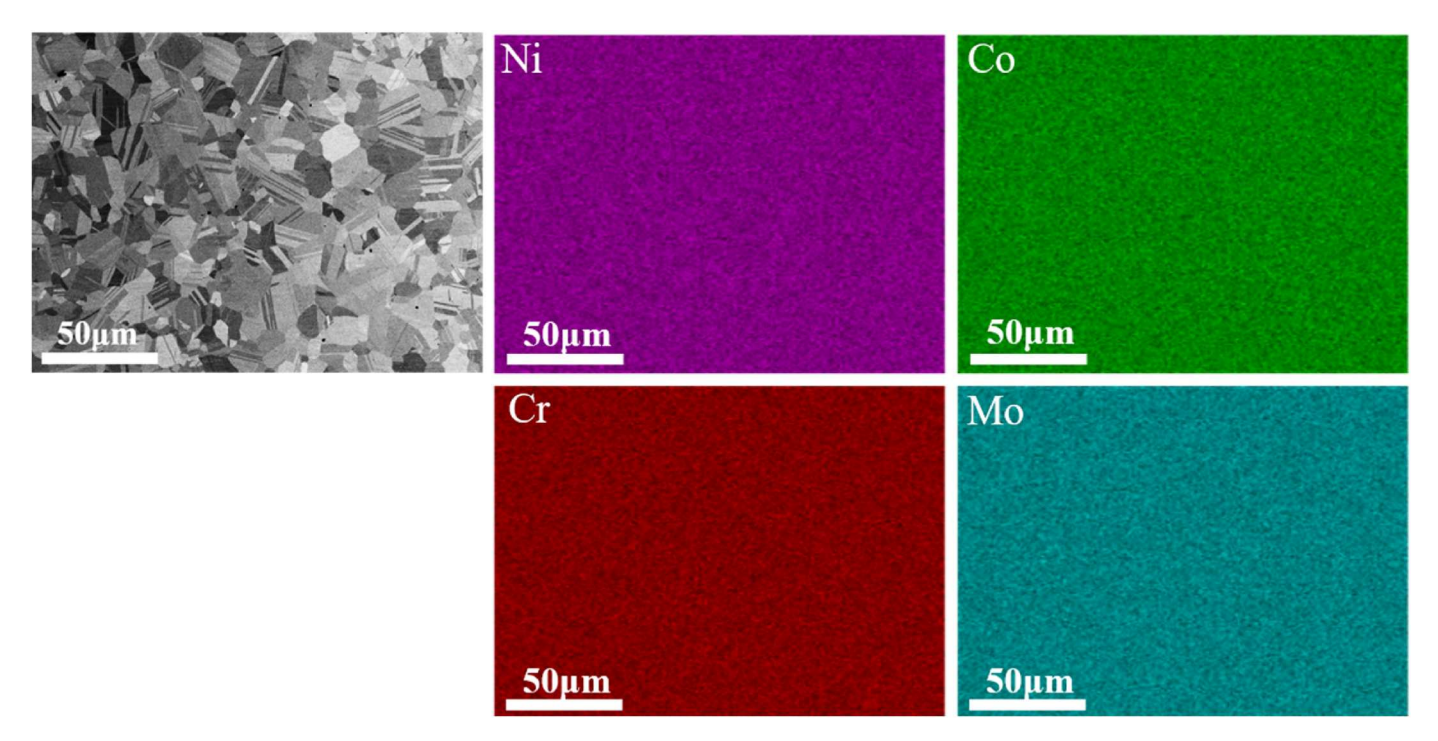


Fig. 3. Elemental mapping of the recrystallized Mo-MEA.

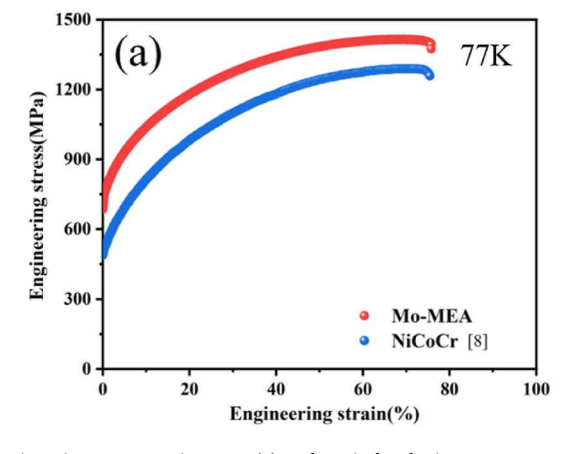
**Table 1** Composition of the Mo-MEA.

	Composition (at.%)			
	Ni	Co	Cr	Мо
Nominal Experimental	$28.2 \\ 28.1 \pm 0.1$	$37.6 \\ 36.9 \pm 0.2$	$28.2 \\ 28.8 \pm 0.4$	$6\\6.2\pm0.2$

Nevertheless, the solubility limit of Mo within the equiatomic NiCoCr MEA is about 6 % at 1100 °C, a constraint driven by the thermodynamically predicted formation of sigma phase, as illustrated in the computed phase diagram for the (NiCoCr)<sub>100-x</sub>Mo<sub>x</sub> alloy system (0  $\leq$  X  $\leq$  20) depicted in Fig. 1b. Furthermore, the emergence of the brittle sigma phase markedly compromises the ductility of the NiCoCr MEA at both RT and cryogenic temperatures [19–21,23]. Concurrently, the segregation of Mo restricts the fine-tuning of the SFE within the NiCoCr matrix.

In the present work, we added the effective solid-solution

strengthening element, Mo, into the Ni<sub>30</sub>Co<sub>40</sub>Cr<sub>30</sub> MEA to reduce SFE. Instead of the equiatomic NiCoCr MEA, the choice of the Ni<sub>30</sub>Co<sub>40</sub>Cr<sub>30</sub> MEA as the base alloy is due to the increasing solution limit of Mo in the low Cr-contained Ni-Co-Cr MEA and thus the Ni<sub>30</sub>Co<sub>40</sub>Cr<sub>30</sub> MEA with a similar SFE as the equiatomic NiCoCr MEA (Fig. 1a) enables the SFE tuning in a relatively broad range to obtain a metastable state. We further calculated the phase diagram of  $(Ni_{0.3}Co_{0.4}Cr_{0.3})_{100\text{-}x}Mo_x$  (0  $\leq$  X  $\leq$  20) (Fig. 1c). Compared with the (NiCoCr)<sub>100-x</sub>Mo<sub>x</sub> (0  $\leq$  X  $\leq$  20), the solubility of Mo in Ni<sub>30</sub>Co<sub>40</sub>Cr<sub>30</sub> at 1100 °C is increased. The nonequiatomic (Ni<sub>0.3</sub>Co<sub>0.4</sub>Cr<sub>0.3</sub>)<sub>94</sub>Mo<sub>6</sub> MEA (denoted as Mo-MEA hereafter) was fabricated by arc melting in the present work. Its tensile properties were evaluated at the cryogenic temperature of 77 K. The newly developed non-equiatomic Mo-MEA exhibited superior mechanical performance, compared to the equiatomic NiCoCr MEA, with significant improvements in the yield strength and ultimate tensile strength, as well as a slight increase in ductility. And the deformation mechanisms in this non-equiatomic Mo-MEA were systematically studied by electron backscattered diffraction (EBSD) and transmission electron microscopy (TEM).



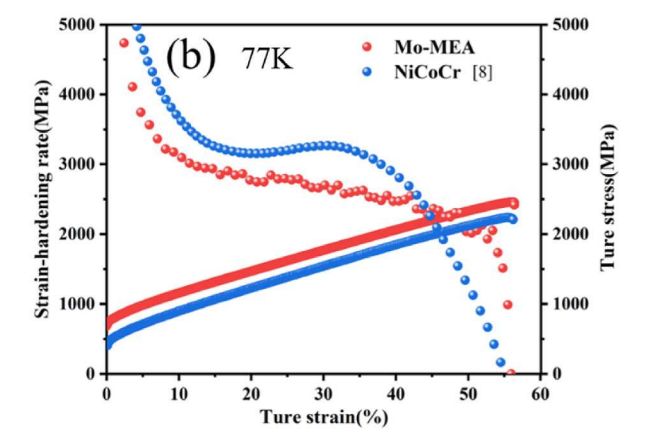


Fig. 4. Engineering stress-strain curve (a) and strain-hardening rate vs. true strain (b) of the Mo-MEA. Experimental data of the widely-studied equiatomic NiCoCr from Ref. [8] was added for a comparison.

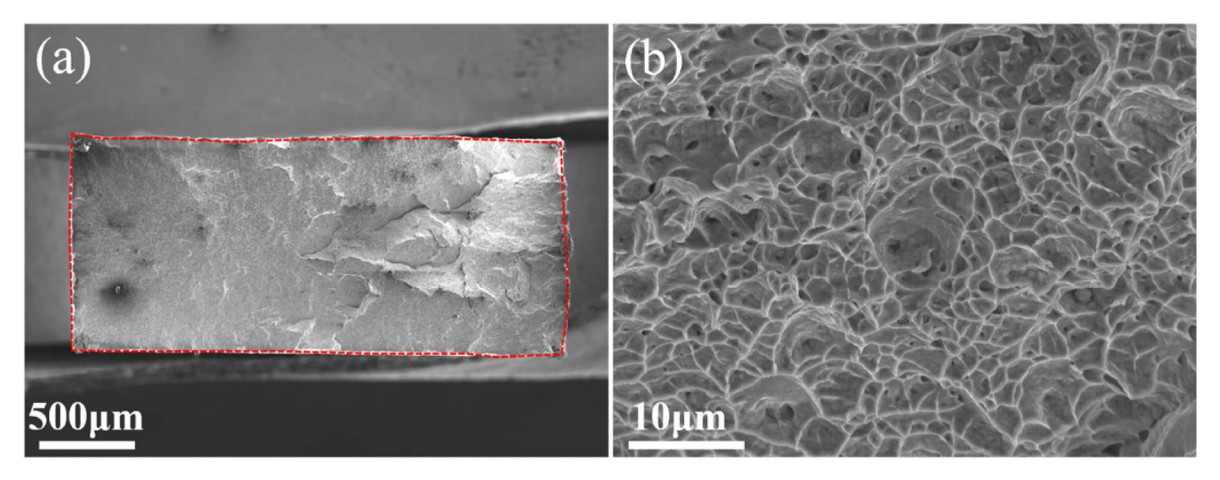


Fig. 5. Fractography of the Mo-MEA deformed at 77 K.

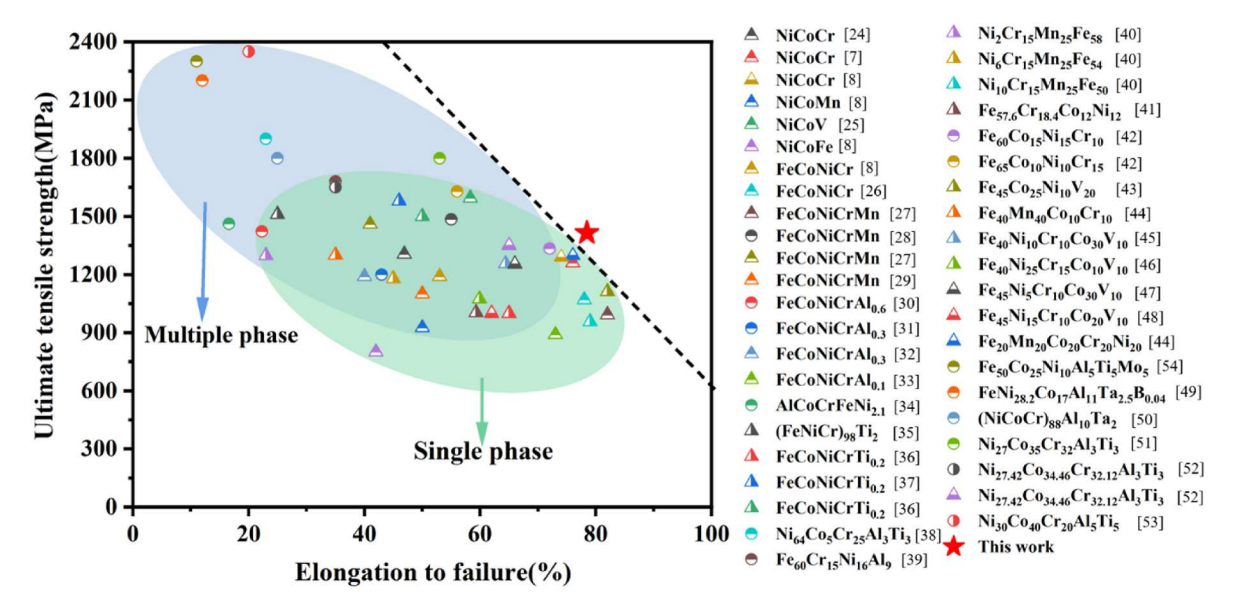


Fig. 6. Ultimate tensile strength vs. elongation for different MEAs and HEAs deformed at 77 K [7,8,24–54]. Circle symbols refers to alloys with multiple phase and triangle symbols represents single phase alloys.

#### 2. Methodology

The Mo-MEA ingot was synthesized by arc melting Ni, Co, Cr and Mo (a purity of 99.9 wt%, ZhongNuo Advanced Materials (Beijing) Technology Co., Ltd) in high-purity argon gas. To ensure composition uniformity, the ingot was flipped and remelted at least six times, then cast into a Cu mold with dimensions of  $8 \times 8 \times 80$  mm<sup>3</sup>. The as-cast sample was sealed in a vacuum quartz tube, homogenized for 24 h at 1473 K, and water-quenched. The homogenized sample was cold-rolled along the longitudinal direction with an 80 % thickness reduction from 8.0 to 1.5 mm. Flat dog-bone-shaped tensile specimens with a gauge length of 20 mm and a thickness of 1.5 mm were cut from the cold-rolled sheet using electrical discharge machining along the rolling direction. The tensile specimens were annealed at 1273 K for 1 h and water-quenched to obtain a fully recrystallized microstructure. Tensile tests were performed at 77 K in liquid nitrogen environment on a 10T mechanical testing machine (CMT-5105, SENS) at a strain rate of  $1\times10^{-3}\,\text{s}^{-1}$ . Prior to testing, the specimens were immersed in liquid nitrogen for 20 min to reach an equilibrium temperature. To study the microstructure evolution during the plastic deformation, beside the fractured specimen two more tensile specimens were deformed to different engineering strain of 5 % and 25 %, respectively.

Microstructure and composition were characterized by using a field-emission scanning electron microscope (AMBER, TESCAN) equipped with EBSD and energy dispersive X-ray spectrometer (EDX). TEM operated at 200 V (Talos F200X G2) was utilized to study deformation mechanisms. The annealed samples were ground up to 2000 grit, mechanically polished in a colloidal SiO $_2$  suspension of 0.05  $\mu m$ , and electrolytically polished in a solution of  $\rm H_2SO_4$  and CH $_3OH$  (a volume ratio of 1: 4) for the EBSD characterization. The TEM thin foils were prepared by gallium-focused ion beam (AMBER, TESCAN).

## 3. Results

#### 3.1. Microstructure

The microstructure of the annealed Mo-MEA is presented in Fig. 2a, showing a fully recrystallized microstructure with equiaxed grains randomly distributed throughout. Preferred grain orientations along <001> and <101> was observed for the recrystallized grains, as indicated by the inset in Fig. 2a. It is worth to mention that the error for the texture analysis can be large due to the limited statistical result. Additionally, a high density of annealing twins was observed, which suggests that the non-equiatomic Mo-MEA possesses a low SFE. The grain-size

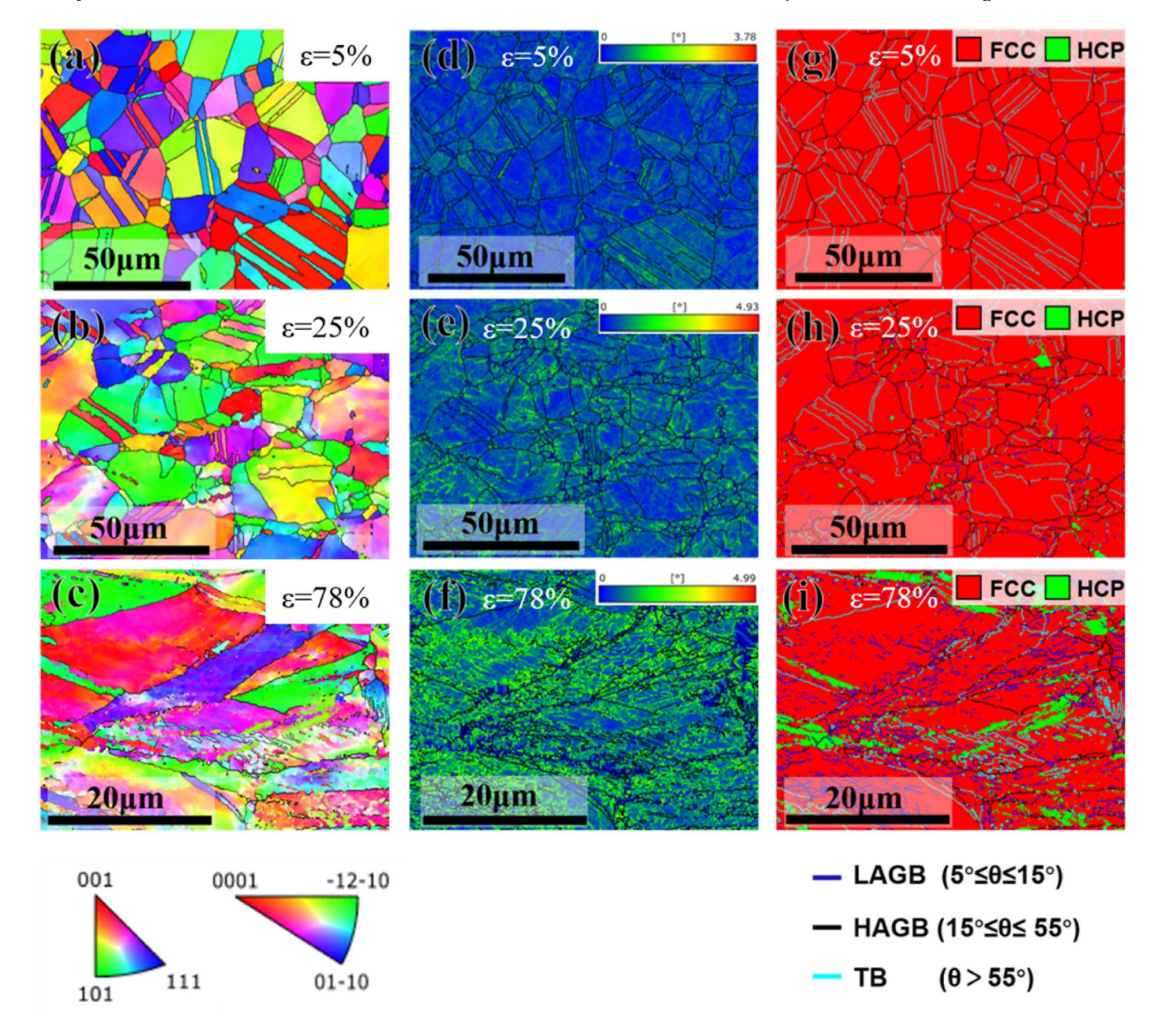


Fig. 7. EBSD analysis of Mo-MEA specimens deformed to different engineering strain. (a–c) IPF, (d–f) Kernal average misorientation maps, and (g–i) phase maps. Loading axis is parallel to the height direction of the EBSD images.

distribution is shown in Fig. 2b, with an average grain size of  $18.5~\mu m$ . Compositional homogeneity of the Mo-MEA was examined by EDX elemental mapping, as shown in Fig. 3. No apparent elemental segregation was found in the Mo-MEA. A quantitative characterization of elements in the Mo-MEA was obtained by EDX point analysis. Table 1 compares the nominal composition with the experimental one. It can be seen that the experimental composition agrees well with the nominal one. And the small deviation in composition further proves the homogeneous composition in the Mo-MEA.

## 3.2. Mechanical properties

The mechanical properties of the recrystallized Mo-MEA at 77 K were investigated through uniaxial tension. Fig. 4a presents the engineering stress-strain curve for the Mo-MEA, along with the curve for the commonly studied equiatomic NiCoCr MEA [8] for comparison. Compared to the equiatomic NiCoCr MEA, the Mo-MEA exhibited a

substantial increase in yield strength (68 % increase from 407 to 685 MPa), and a decent enhancement in the ultimate tensile strength (10 % increase from 1289 to 1415 MPa). Despite these remarkable improvements in strength, the ductility of the Mo-MEA was not compromised, as evidenced by the marginal increase in the elongation from 75 % to 78.45 %. Accordingly, a remarkable strength-ductility synergy was achieved in the Mo-MEA at 77 K. Fig. 4b displays the work-hardening behavior of the Mo-MEA as a function of the true strain. Different from the NiCoCr MEA with three-stage work hardening during the uniform plastic deformation process, the work-hardening rate of the Mo-MEA shows a two-stage decrease, i.e., a sharp decline at the initial stage of plastic deformation (prior to the true strain of  $\sim$ 6 %) followed by a slow reduction until the end of uniform plastic deformation. Fractography of the Mo-MEA was examined by SEM, as shown in Fig. 5. No large macroscopic necking was observed (Fig. 5a), but a high density of dimples (Fig. 5b) was formed on the fracture surface, revealing a characteristic of ductile fracture.

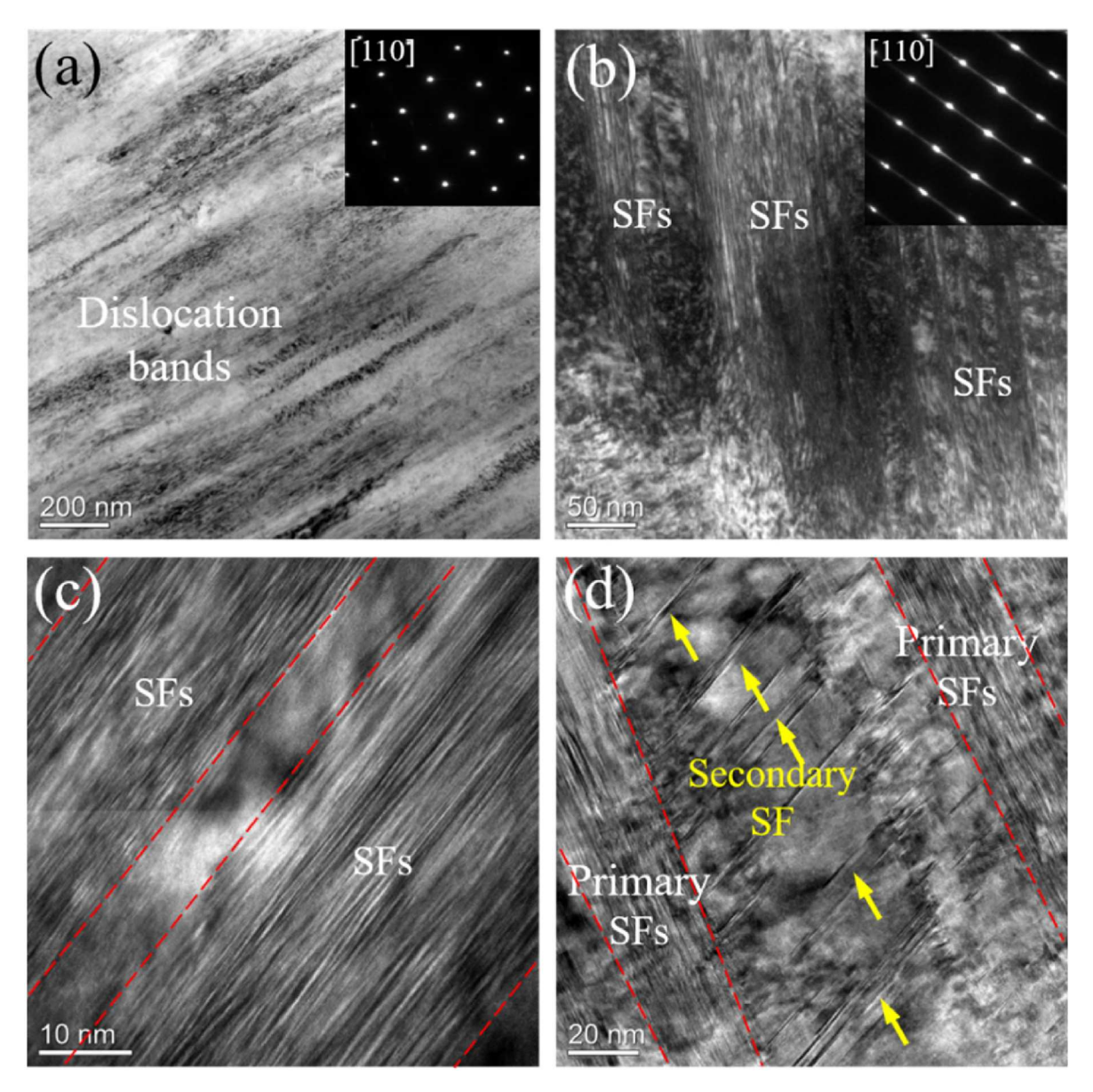


Fig. 8. Bright-field TEM images of different deformed grains containing dislocation bands (a), stacking faults (b) and hierarchical SF microstructures (d) in the fractured specimen. (c) High-resolution TEM image of SFs in (b). All images were taken along the [110] zone axis. The inset in (a) and (b) shows the SADPs of dislocation bands and SFs, respectively.

Fig. 6 compares the ultimate tensile strength and elongation of various MEAs and high-entropy alloys (HEAs) deformed at the cryogenic temperature of 77 K. Obviously, our newly designed Mo-MEA exhibits an excellent combination of high strength and ductility at such an extremely low temperature. The ultimate tensile strength of the Mo-MEA is comparable to that of the precipitate-strengthened FeCo-NiCrTi<sub>0.2</sub> HEAs, whereas its ductility surpasses other single-phase HEAs, including the most damage-tolerant equiatomic NiCoCr MEA reported to date [9]. Therefore, our Mo-MEA possesses a great potential for applications requiring extraordinary strength-ductility synergy at cryogenic temperatures.

# 4. Discussion

To investigate the microstructural origin of the mechanical behaviors, we studied deformation microstructure of the interrupted tensile-deformed samples by EBSD technique (Fig. 7). Fig. 7a–c shows the IPFs of the Mo-MEA specimens deformed to the strain of 5 %, 25 % and 78 % (fracture), respectively. At a tensile strain of 5 %, grain orientation

change is hardly detected and a few of small deformation twins occurred (Fig. 7a). With a further increase of strain up to 25 %, grain orientation change dramatically increases especially near the grain boundaries, indicating the activation of multiple slip systems, but meanwhile deformation twins are not increased much (Fig. 7b). For the fractured specimen, large orientation change happens across each grain and grains were elongated, but still deformation twins remain with a low density. Fig. 7d-f qualitatively evaluate the density of geometrically necessary dislocations for the specimens deformed to different strain. At the low strain of 5 %, dislocations are distributed in a relatively random fashion but confined by grain and twin boundaries (Fig. 7d). When the specimen was deformed to 25 %, dislocations distribute heterogeneously to form cells and networks (Fig. 7e). In the fractured sample, a high density of dislocations was formed in each grain to hinder their further movement (Fig. 7f). Moreover, phase change was examined, as shown in the phase maps in Fig. 7g-i. With the increase of strain, the FCC-to-HCP phase transformation increases, but the fraction of HCP phase is relatively low, indicating that TRIP is not the dominant deformation mechanism. Note that low angle grain boundaries (LAGBs) started to form at the medium

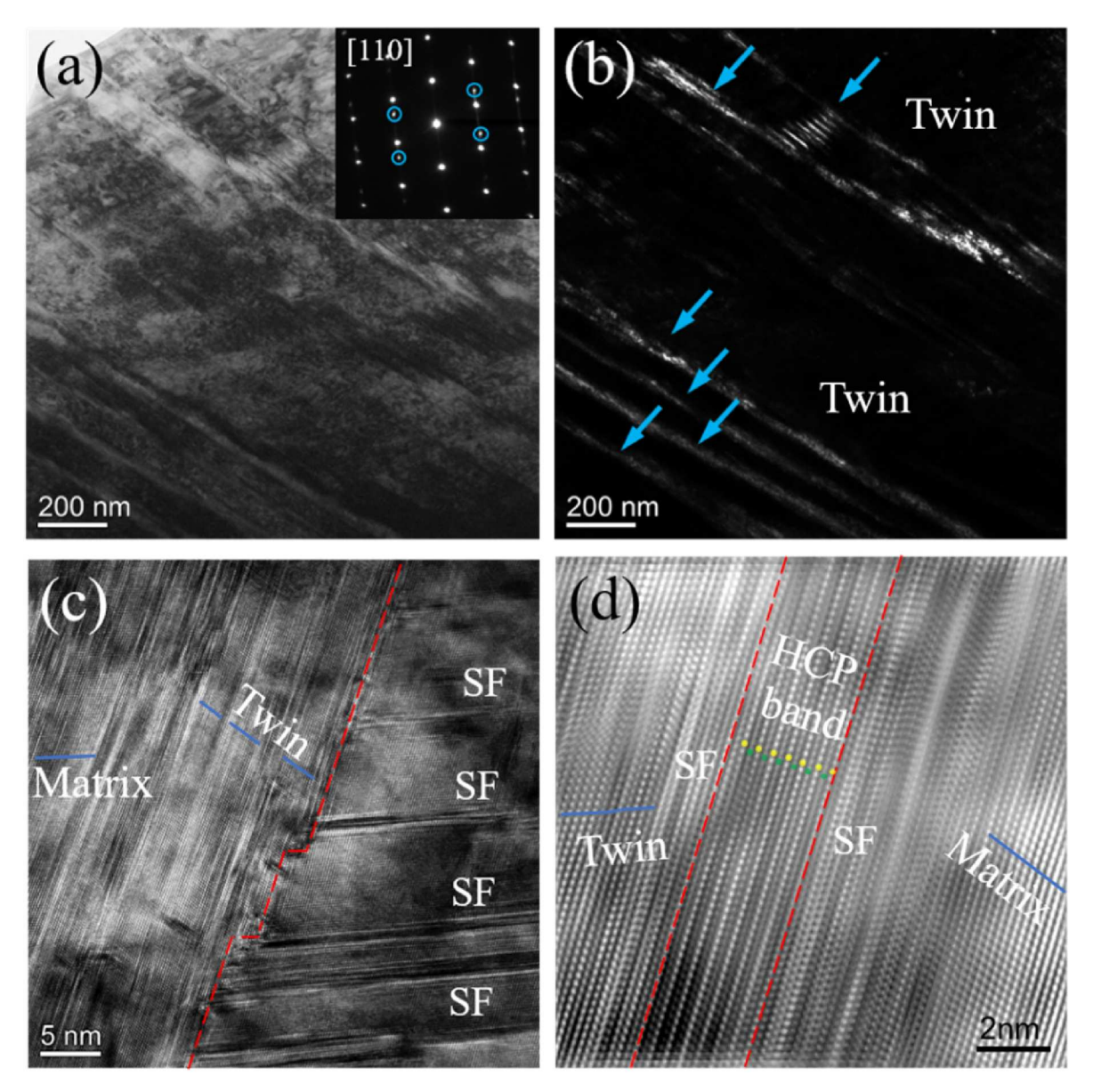


Fig. 9. Deformation structure of the fractured specimen. (a) Bright-field TEM image of deformation twins. The inset SADP reveals diffraction spots from twinning (circle in blue). (b) Dark-field TEM of deformation twins. (c) High-resolution TEM of an interaction between the deformation twin and SFs. (d) High-resolution TEM image of HCP lamellae.

strain of 25 %, as indicated by blue lines in Fig. 7h, and increased dramatically in the fractured samples (Fig. 7i).

To further understand the deformation mechanisms of the Mo-MEA, the deformation substructures of the fractured specimen were extensively studied by TEM. Dislocation bands were observed in some deformed grains (Fig. 8a). The selected area diffraction pattern (SADP) in the inset of Fig. 8a clearly shows that only diffraction spots from the FCC matrix occur, revealing the dislocation-controlled deformation mechanism in some grains. A high density of bundles formed by SF were found among the dislocation networks in most of deformed grains (Fig. 8b). The streaking lines in the SADP taken along the [110] zone axis demonstrates the characteristic of SFs. The SF bundles have a varying width and interspacing in tens of nanometers (Fig. 8c). The narrow interspace between SF bundles was observed to confine the motion of other deformation defects, as demonstrated by the hierarchical SF structure (Fig. 8d). The primary SF bundles apparently serve as barriers to hinder the penetration of the secondary SFs. The intersection of primary and secondary SFs refined the grain into nanosized regions for the dislocation movement, leading to a strong dynamic Hall-Petch

effect [55].

In addition to the dislocation and SF deformation mechanisms, a TWIP deformation mechanism was also detected, as demonstrated in Fig. 9. The SADP in Fig. 9a shows extra diffraction spots (circled in blue), which indicate typical twinning regions. The dark-field TEM image in Fig. 9b reveals the formation of nanosized deformation twins contributing to the twinning diffraction spots. Moreover, complex substructures were formed around deformation-twinning regions, as presented in the high-resolution TEM image of Fig. 9c. On the other hand, the deformation twins act as barriers, hindering the propagation of secondary SFs on different {111} planes at an angle of  $\sim$ 70°. Notice that deformed twins always mixed with SFs in the deformed specimen. Furthermore, HCP bands with tens of atomic layers are formed near the boundary of deformation twins and SFs, as demonstrated in Fig. 9d, revealing the activation of a TRIP deformation mechanism.

The detection of the HCP phase at 77 K suggests that the thermodynamically stable phase of the Mo-MEA at cryogenic temperatures is the HCP phase, and the deformation twins are metastable. Recent ab initio calculation [15] shows that the SFE of (NiCoCr)<sub>97</sub>Mo<sub>3</sub> MEA is

 $-40.4~\rm mJ/m^2$  at 0 K, lower than the one of the NiCoCr MEA [12]. Moreover, ab initio calculations [12] found that the SFE of the Ni $_{30}$ C- $_{040}$ Cr $_{30}$  MEA is about the same as the one of the NiCoCr MEA. Therefore, the SFE of the Ni $_{30}$ Co $_{40}$ Cr $_{30}$  MEA is expected to be negative after the addition of Mo. The SFE corresponds to the energy difference between the HCP and FCC structures. Thus, the negative SFE of the Mo-MEA implies the thermodynamically stable HCP phase at low temperatures.

The negative SFE [15] suggests that the TRIP mechanism should dominate deformation in the Mo-MEA at 77 K. However, the observation of SFs and twinning in the Mo-MEA deformed at 77 K contrasts this projection. In fact, the intrinsic SF in the FCC structure can be treated as a two-layer embryo of the HCP structure. But the formation of deformation twins is the consequence of the competition between the energy barriers for SF,  $\overline{\gamma}_{SF}(\theta) = \gamma_{usf}/\cos\theta$ , and twinning,  $\overline{\gamma}_{TW}(\theta) = (\gamma_{utf} - \gamma_{isf})/$  $\cos \theta$  [56]. Here,  $\gamma_{usf}$ ,  $\gamma_{utf}$ , and  $\gamma_{isf}$  are unstable SFE, unstable twin fault energy, and intrinsic SFE, respectively, and  $\theta$  indicates the effect of grain orientation relative to the direction of the resolved shear stress. Through ab initio calculations. Yang et al. [57] found that the Ni<sub>30</sub>Co<sub>40</sub>Cr<sub>30</sub> MEA at 77 K has a slightly smaller SF energy barrier than the twinning energy barrier,  $\bar{\gamma}_{SF} - \bar{\gamma}_{TW} = -14 \text{ mJ/m}^2$ . Thus, HCP phase should be preferred. However, it should be noted that the effect of affine deformation is not considered in this calculation of energy-barrier difference. Note that in a solid under affine deformation, the local elastic strain is homogeneous across the whole body and equivalent to the macroscopic elastic strain. Since a critical resolved shear stress is needed to shear the {111} atomic layers, the influence of the affine strain on the energy barriers should be evaluated. Here, we roughly estimated the influence of the affine strain on  $\overline{\gamma}_{SF} - \overline{\gamma}_{TW}$  of the Ni<sub>30</sub>Co<sub>40</sub>Cr<sub>30</sub> MEA based on the NiCoCr MEA case since their SFE difference is relatively small. Combining the measured critical twinning shear stress of 260 MPa [6] and shear modulus of 87 GPa [8] for the polycrystal NiCoCr MEA, the critical twinning shear strain for the single-crystal NiCoCr MEA is ~0.93 %. Moreover, Huang et al. [13] calculated that in the NiCoCr MEA applying an affine strain from 0.8 % to 1.2 % can increase the value of  $\overline{\gamma}_{SF} - \overline{\gamma}_{TW}$  by ~15 mJ/m<sup>2</sup> at 77 K. Thus, the estimated  $\overline{\gamma}_{SF}-\overline{\gamma}_{TW}$  for the  $Ni_{30}Co_{40}Cr_{30}$  MEA at 77 K is very close to 0 mJ/m<sup>2</sup>, suggesting that the energy barrier for the FCC-to-HCP transformation is comparable to the twinning barrier. Similar to the Ni<sub>30</sub>Co<sub>40</sub>Cr<sub>30</sub> MEA, the Mo-MEA is marginally situated at the boundary of unconventional metastable twinning and TRIP deformation at 77 K, resulting in the coexistence of TRIP deformation and twinning. Different from our newly-designed Mo-MEA with comparable values of  $\overline{\gamma}_{SF}$  and  $\overline{\gamma}_{TW}$ , a recent investigation [22] of the Mo-doped  $Ni_{15}Cr_{25}Co_{40}Fe_{15}Mo_5$  HEA with a large difference between  $\overline{\gamma}_{SF}$  and  $\bar{\gamma}_{TW}$ , -28 mJ/m<sup>2</sup>, shows only stacking faults and TRIP deformation mechanism without the formation of deformation twins.

# 5. Conclusion

To summarize, we have successfully developed an FCC nonequiatomic Mo-MEA with a synergy of excellent strength and ductility at 77 K, achieved through multimodal deformation mechanisms, including dislocations, stacking faults, twinning, and FCC-to-HCP phase transformation. Compared to the most fracture-tolerant equiatomic NiCoCr MEA reported [9], the non-equiatomic Mo-MEA demonstrated 68 % and 10 % increase in yield and ultimate tensile strength, respectively, without compromising ductility. Our TEM analysis revealed that the dominant deformation mechanisms are dislocations and stacking faults, and meanwhile the formation of hierarchical stacking fault and twin structures further refines the grains, leading to a strong dynamic Hall-Petch effect. Although the thermodynamically stable phase of the non-equiatomic Mo-MEA is HCP, the comparable energy barriers between SFs and twinning suppresses the formation of a large amount of HCP phase, thus preventing premature fracture in the metastable Mo-MEA. These findings underscore the importance of the activation and precise control of multimodal deformation mechanisms in achieving

optimal mechanical properties.

#### **Declaration of competing interest**

The authors declare the following financial interests/personal relationships which may be considered as potential competing interests: Yang Tong reports financial support was provided by National Natural Science Foundation of China (Grant Nos. 52001272, 52371164). Yang Tong reports financial support was provided by Taishan Scholars Program of Shandong Province (tsqn202103052). Yang Tong reports financial support was provided by Yantai city matching fund for Taishan Scholars Program of Shandong Province. Shuying Chen reports financial support was provided by National Natural Science Foundation of China (Grant Nos. 52001271, 52371163). Fanchao Meng reports financial support was provided by Natural Science Foundation of Shandong Province (Grant No. ZR2021QE110). Peter Liaw reports financial support was provided by National Science Foundation. Peter Liaw reports financial support was provided by US Army Research Office.

#### Acknowledgement

Y.T. gratefully acknowledges the financial support by the National Natural Science Foundation of China (Grant No. 52001272, 52371164), Taishan Scholars Program of Shandong Province (tsqn202103052), Yantai city matching fund for Taishan Scholars Program of Shandong Province, and Top Discipline in Materials Science of Shandong Province. S.C. acknowledges the support by the National Natural Science Foundation of China (Grant No. 52001271, 52371163). F.M. appreciates the support from the Natural Science Foundation of Shandong Province (Grant No. ZR2021QE110). P.K.L. very much appreciates the support from (1) the National Science Foundation (DMR– 1611180, 1809640, and 2226508) and (2) the US Army Research Office (W911NF-13–1-0438 and W911NF-19–2-0049).

#### References

- Byun TS, Hashimoto N, Farrell K. Temperature dependence of strain hardening and plastic instability behaviors in austenitic stainless steels. Acta Mater 2004;52: 3889–99.
- [2] Umezawa O. Review of the mechanical properties of high-strength alloys at cryogenic temperatures. Mater Performance Charact 2021;10:3–15.
- [3] Yeh J-W. Alloy design strategies and future trends in high-entropy alloys. JOM 2013:65:1759–71.
- [4] Yeh J-W. Physical metallurgy of high-entropy alloys. JOM 2015;67:2254–61.
- [5] Gludovatz B, Hohenwarter A, Thurston KVS, Bei H, Wu Z, George EP, et al. Exceptional damage-tolerance of a medium-entropy alloy CrCoNi at cryogenic temperatures. Nat Commun 2016;7:10602.
- [6] Laplanche G, Kostka A, Reinhart C, Hunfeld J, Eggeler G, George EP. Reasons for the superior mechanical properties of medium-entropy CrCoNi compared to highentropy CrMnFeCoNi. Acta Mater 2017;128:292–303.
- [7] Miao J, Slone CE, Smith TM, Niu C, Bei H, Ghazisaeidi M, et al. The evolution of the deformation substructure in a Ni-Co-Cr equiatomic solid solution alloy. Acta Mater 2017;132:35–48.
- [8] Wu Z, Bei H, Pharr GM, George EP. Temperature dependence of the mechanical properties of equiatomic solid solution alloys with face-centered cubic crystal structures. Acta Mater 2014;81:428–41.
- [9] Liu D, Yu Q, Kabra S, Jiang M, Forna-Kreutzer P, Zhang R, et al. Exceptional fracture toughness of CrCoNi-based medium- and high-entropy alloys at 20 kelvin. Science 2022;378:978–83.
- [10] Gludovatz B, Hohenwarter A, Thurston KVS, Bei H, Wu Z, George EP, et al. Exceptional damage-tolerance of a medium-entropy alloy CrCoNi at cryogenic temperatures. Nat Commun 2016;7:10602.
- [11] Gludovatz B, Hohenwarter A, Catoor D, Chang EH, George EP, Ritchie RO. A fracture-resistant high-entropy alloy for cryogenic applications. Science 2014; 345:1153–8.
- [12] Yang Z, Lu S, Tian Y, Gu Z, Sun J, Vitos L. Theoretical and experimental study of phase transformation and twinning behavior in metastable high-entropy alloys. J Mater Sci Technol 2022;99:161–8.
- [13] Huang S, Huang H, Li W, Kim D, Lu S, Li X, et al. Twinning in metastable high-entropy alloys. Nat Commun 2018;9:2381.
- [14] Yoshida S, Ikeuchi T, Bai Y, Tsuji N. Effect of cobalt-content on mechanical properties of non-equiatomic Co-Cr-Ni medium entropy alloys. Mater Trans 2020; 61:587-95

- [15] Chang R, Fang W, Yan J, Yu H, Bai X, Li J, et al. Microstructure and mechanical properties of CoCrNi-Mo medium entropy alloys: experiments and first-principle calculations. J Mater Sci Technol 2021;62:25–33.
- [16] Chan S-N, Hsueh C-H. Effects of La addition on the microstructure and mechanical properties of CoCrNi medium entropy alloy. J Alloy Compd 2022;894:162401.
- [17] Hong X, Hsueh C-H. Effects of yttrium addition on microstructures and mechanical properties of CoCrNi medium entropy alloy. Intermetallics 2022;140:107405.
- [18] Lin Y-S, Lu Y-C, Hsueh C-H. Strengthening of CoCrNi medium entropy alloy with gadolinium additions. Vacuum 2023;211:111969.
- [19] Li N, Gu J, Gan B, Qiao Q, Ni S, Song M. Effects of Mo-doping on the microstructure and mechanical properties of CoCrNi medium entropy alloy. J Mater Res 2020;35: 2726–36
- [20] Chang R, Fang W, Yu H, Bai X, Zhang X, Liu B, et al. Heterogeneous banded precipitation of (CoCrNi)93Mo7 medium entropy alloys towards strength–ductility synergy utilizing compositional inhomogeneity. Scripta Mater 2019;172:144–8.
- [21] He J, Makineni SK, Lu W, Shang Y, Lu Z, Li Z, et al. On the formation of hierarchical microstructure in a Mo-doped NiCoCr medium-entropy alloy with enhanced strength-ductility synergy. Scripta Mater 2020;175:1–6.
- [22] Wei D, Li X, Schönecker S, Jiang J, Choi W-M, Lee B-J, et al. Development of strong and ductile metastable face-centered cubic single-phase high-entropy alloys. Acta Mater 2019;181:318–30.
- [23] Zhang H, Ren Z, Tong Y, Hu Y, Ji X, Yang L, et al. Introduction of nanotwins into nanoprecipitations strengthened CoCrNiMo0.2 alloy to achieve strength and ductility trade-off: a comparative research. J Mater Sci Technol 2023;156:172–82.
- [24] Han B, Zhang C, Feng K, Li Z, Zhang X, Shen Y, et al. Additively manufactured high strength and ductility CrCoNi medium entropy alloy with hierarchical microstructure. Mater Sci Eng A 2021;820:141545.
- [25] Han Z, Ding C, Liu G, Yang J, Du Y, Wei R, et al. Analysis of deformation behavior of VCoNi medium-entropy alloy at temperatures ranging from 77 K to 573 K. Intermetallics 2021;132:107126.
- [26] Liu J, Guo X, Lin Q, He Z, An X, Li L, et al. Excellent ductility and serration feature of metastable CoCrFeNi high-entropy alloy at extremely low temperatures. Sci China Mater 2019;62:853–63.
- [27] Sun SJ, Tian YZ, An XH, Lin HR, Wang JW, Zhang ZF. Ultrahigh cryogenic strength and exceptional ductility in ultrafine-grained CoCrFeMnNi high-entropy alloy with fully recrystallized structure. Mater Today Nano 2018;4:46–53.
- [28] Shim SH, Moon J, Pouraliakbar H, Lee BJ, Hong SI, Kim HS. Toward excellent tensile properties of nitrogen-doped CoCrFeMnNi high-entropy alloy at room and cryogenic temperatures. J Alloy Compd 2022;897:163217.
- [29] Kireeva IV, Chumlyakov YI, Vyrodova AV, Pobedennaya ZV, Karaman I. Effect of twinning on the orientation dependence of mechanical behaviour and fracture in single crystals of the equiatomic CoCrFeMnNi high-entropy alloy at 77K. Mater Sci Eng A 2020;784:139315.
- [30] Li Q, Zhang TW, Qiao JW, Ma SG, Zhao D, Lu P, et al. Mechanical properties and deformation behavior of dual-phase Al0.6CoCrFeNi high-entropy alloys with heterogeneous structure at room and cryogenic temperatures. J Alloy Compd 2020; 816:152663.
- [31] Kireeva IV, Chumlyakov YI, Pobedennaya ZV, Vyrodova AV. Effect of γ'-phase particles on the orientation and temperature dependence of the mechanical behaviour of Al0.3CoCrFeNi high-entropy alloy single crystals. Mater Sci Eng A 2020:772:138772.
- [32] Kireeva IV, Chumlyakov YI, Pobedennaya ZV, Vyrodova AV, Kuksgauzen IV, Kuksgauzen DA. Orientation and temperature dependence of a planar slip and twinning in single crystals of Al0.3CoCrFeNi high-entropy alloy. Mater Sci Eng A 2018;737-47-60
- [33] Li J, Lu K, Wang Y, Zhang Y, Ma X, Chen J, et al. Exceptional cryogenic strength and sufficient ductility of a nanotwinned high-entropy alloy fabricated by cryogenic multi-directional compression. J Alloy Compd 2023;931:167533.
- [34] Bhattacharjee T, Zheng R, Chong Y, Sheikh S, Guo S, Clark IT, et al. Effect of low temperature on tensile properties of AlCoCrFeNi2.1 eutectic high entropy alloy. Mater Chem Phys 2018;210:207–12.
- [35] Ma D, Xu H, Ding J, Shen Y, Zhang T. Improved strength and ductility of Ti2 (CrFeNi)98 multi-principal element alloy at cryogenic temperature with deformation twins induced by BCC precipitates. Mater Sci Eng A 2023;862:144489.

- [36] Yuan J, Zhang H, Wang Z, Han P, Qiao J. Contribution of coherent precipitates on mechanical properties of CoCrFeNiTi0.2 high-entropy alloy at room and cryogenic temperatures. Intermetallics 2023;154:107820.
- [37] Tong Y, Chen D, Han B, Wang J, Feng R, Yang T, et al. Outstanding tensile properties of a precipitation-strengthened FeCoNiCrTi0.2 high-entropy alloy at room and cryogenic temperatures. Acta Mater 2019;165:228–40.
- [38] Shi CX, Du XH, Zhang JY, Yang MC, Zu RF, Gai YH, et al. Making a coherent L12-nano-precipitates-reinforced Ni-based alloy ultrastrong and ductile by constructing dual heterogeneous structures. Intermetallics 2023;159:107914.
- [39] Wei R, Gao Q, Zhang X, Zhang K, Wang L, Han Z, et al. Heterogeneous-structure-induced ultrahigh strength and ductility in a metastable dual-phase Fe60Cr15Ni16Al9 medium entropy alloy. Mater Sci Eng A 2023;867:144710.
- [40] Wang H, Zhang K, Chen L, Gao Q, Zhao X, Chen C, et al. Strengthening Fe50+ xMn25Cr15Ni10-x medium-entropy alloys by Ni/Fe replacement: experiments and molecular dynamics study. Intermetallics 2023;155:107833.
- [41] Zhong W, Hayakawa S, Xu H, An K, Borisevich AY, Cicotte JL, et al. Deciphering the multiple deformation mechanisms responsible for sustained work hardening in a FeCrCoNi medium entropy alloy. Int J Plast 2023;167:103663.
- [42] Zhang K, Zhang X, Zhang E, Wei R, Wang L, Chen J, et al. Strengthening of ferrous medium entropy alloys by promoting phase transformation. Intermetallics 2021; 136:107265.
- [43] Li YX, Nutor RK, Zhao QK, Zhang XP, Cao QP, Sohn SS, et al. Unraveling the deformation behavior of the Fe45Co25Ni10V20 high entropy alloy. Int J Plast 2023;165:103619.
- [44] Seol JB, Bae JW, Kim JG, Sung H, Li Z, Lee HH, et al. Short-range order strengthening in boron-doped high-entropy alloys for cryogenic applications. Acta Mater 2020;194:366–77.
- [45] Kim DG, Jo YH, Yang J, Choi W-M, Kim HS, Lee B-J, et al. Ultrastrong duplex highentropy alloy with 2 GPa cryogenic strength enabled by an accelerated martensitic transformation. Scripta Mater 2019;171:67–72.
- [46] Jang MJ, Kwak H, Lee YW, Jeong Y, Choi J, Jo YH, et al. Plastic deformation behavior of 40Fe-25Ni-15Cr-10Co-10V high-entropy alloy for cryogenic applications. Met Mater Int 2019;25:277-84.
- [47] Jo YH, Yang J, Doh K-Y, An W, Kim DW, Sung H, et al. Analysis of damagetolerance of TRIP-assisted V10Cr10Fe45Co30Ni5 high-entropy alloy at room and cryogenic temperatures. J Alloy Compd 2020;844:156090.
- [48] Jo YH, Doh K-Y, Kim DG, Lee K, Kim DW, Sung H, et al. Cryogenic-temperature fracture toughness analysis of non-equi-atomic V10Cr10Fe45Co20Ni15 highentropy alloy. J Alloy Compd 2019;809:151864.
- [49] Zhang C, Yu Q, Tang YT, Xu M, Wang H, Zhu C, et al. Strong and ductile FeNiCoAl-based high-entropy alloys for cryogenic to elevated temperature multifunctional applications. Acta Mater 2023;242:118449.
- [50] Zhang DD, Zhang JY, Kuang J, Liu G, Sun J. The B2 phase-driven microstructural heterogeneities and twinning enable ultrahigh cryogenic strength and large ductility in NiCoCr-based medium-entropy alloy. Acta Mater 2022;233:117981.
   [51] Zhang DD, Zhang JY, Kuang J, Liu G, Sun J. Superior strength-ductility synergy and
- [51] Zhang DD, Zhang JY, Kuang J, Liu G, Sun J. Superior strength-ductility synergy and strain hardenability of Al/Ta co-doped NiCoCr twinned medium entropy alloy for cryogenic applications. Acta Mater 2021;220:117288.
- [52] Zhang Z, Wang W, Qin S, Yang M, Wang J, Jiang P, et al. Dual heterogeneous structured medium-entropy alloys showing a superior strength-ductility synergy at cryogenic temperature. J Mater Res Technol 2022;17:3262–76.
- [53] Chou TH, Li WP, Chang HW, Cao BX, Luan JH, Huang JC, et al. Suppressing temperature-dependent embrittlement in high-strength medium-entropy alloy via hetero-grain/precipitation engineering. Scripta Mater 2023;229:115377.
- [54] Kwon H, Sathiyamoorthi P, Karthik GM, Asghari-Rad P, Zargaran A, Do H-S, et al. 2.3 GPa cryogenic strength through thermal-induced and deformation-induced body-centered cubic martensite in a novel ferrous medium entropy alloy. Scripta Mater 2021;204:114157.
- [55] Gutierrez-Urrutia I, Raabe D. Dislocation and twin substructure evolution during strain hardening of an Fe-22wt.% Mn-0.6wt.% C TWIP steel observed by electron channeling contrast imaging. Acta Mater 2011;59:6449-62.
- [56] Jo M, Koo YM, Lee B-J, Johansson B, Vitos L, Kwon SK. Theory for plasticity of face-centered cubic metals. Proc Nati Acad Sci 2014;111:6560–5.
- [57] Yang Z, Lu S, Tian Y, Gu Z, Mao H, Sun J, et al. Designing transformation-induced plasticity and twinning-induced plasticity Cr-Co-Ni medium entropy alloys: theory and experiment. 2020. arXiv preprint arXiv:2002.05900.